

## CHANDRA X-RAY STUDY OF GALACTIC SUPERNOVA REMNANT G299.2–2.9

SANGWOOK PARK

Department of Astronomy and Astrophysics, 525 Davey Lab., Pennsylvania State University, University Park, PA. 16802

PATRICK O. SLANE

Harvard-Smithsonian Center for Astrophysics, 60 Garden Street, Cambridge, MA. 02138

JOHN P. HUGHES

Department of Physics and Astronomy, Rutgers University, 136 Frelinghuysen Road, Piscataway, NJ. 08854-8019

KOJI MORI

Department of Applied Physics, University of Miyazaki, 1-1 Gakuen Kibana-dai Nishi, Miyazaki, 889-2192, Japan

AND

DAVID N. BURROWS AND GORDON P. GARMIRE

Department of Astronomy and Astrophysics, 525 Davey Lab., Pennsylvania State University, University Park, PA. 16802

*Accepted for the publication in the Astrophysical Journal (Scheduled on Sep 10, 2007, v666)*

### ABSTRACT

We report on observations of the Galactic supernova remnant (SNR) G299.2–2.9 with the *Chandra X-Ray Observatory*. The high resolution images with *Chandra* resolve the X-ray-bright knots, shell, and diffuse emission extending beyond the bright shell. Interior to the X-ray shell is faint diffuse emission occupying the central regions of the SNR. Spatially-resolved spectroscopy indicates a large foreground absorption ( $N_{\text{H}} \sim 3.5 \times 10^{21} \text{ cm}^{-2}$ ), which supports a relatively distant location ( $d \sim 5$  kpc) for the SNR. The blast wave is encountering a highly inhomogeneous ambient medium with the densities ranging over more than an order of magnitude ( $n_0 \sim 0.1 - 4 \text{ cm}^{-3}$ ). Assuming the distance of  $d \sim 5$  kpc, we derive a Sedov age of  $\tau \sim 4500$  yr and an explosion energy of  $E_0 \sim 1.6 \times 10^{50}$  ergs. The ambient density structure and the overall morphology suggest that G299.2–2.9 may be a limb-brightened partial shell extending to  $\sim 7$  pc radius surrounded by fainter emission extending beyond that to a radius of  $\sim 9$  pc. This suggests the SNR exploded in a region of space where there is a density gradient whose direction lies roughly along the line of sight. The faint central region shows strong line emission from heavy elements of Si and Fe, which is caused by the presence of the overabundant stellar ejecta there. We find no evidence for stellar ejecta enriched in light elements of O and Ne. The observed abundance structure of the metal-rich ejecta supports a Type Ia origin for G299.2–2.9.

*Subject headings:* ISM: individual (G299.2–2.9) — supernova remnants — X-rays: ISM

### 1. INTRODUCTION

High angular resolution imaging spectroscopy with the *Chandra X-Ray Observatory* has revolutionized the study of supernova remnants (SNRs) (e.g., Weisskopf & Hughes 2005 for a recent review); spatially-resolved spectral analysis with arcsecond-scale resolution imaging provides a powerful tool to reveal a number of new and detailed structures in the SNRs. We continue such an X-ray study of SNRs with the *Chandra* observation of SNR G299.2–2.9.

The Galactic SNR G299.2–2.9 is one of the handful number of SNRs that were discovered in X-rays with the *ROSAT* all sky survey (Busser et al. 1995). The X-ray morphology reported with the previous X-ray detectors on board *Einstein*, *ROSAT*, and *ASCA* appeared to be “centrally-enhanced” with a partial shell-like structure (Busser et al. 1995; Slane et al. 1996; Bai & Wang 2000). The X-ray spectrum was dominated by thermal emission without evidence for

nonthermal synchrotron emission from the embedded pulsar wind nebula (PWN) at the SNR center (Bai & Wang 2000). A thermal composite SNR was thus suggested for G299.2–2.9, with centrally-enhanced X-ray emission produced by thermal evaporation of cloudlets (White & Long 1991). Although there were some controversial interpretations of the SNR dynamics (young and nearby vs. middle-aged and distant) with the early *ROSAT* PSPC data (Busser et al. 1996), subsequent works found that a model assuming a middle-age ( $\tau \sim 6600$  yr) SNR at a distance of  $d \sim 5$  kpc self-consistently produces the observed X-ray and IR fluxes (Slane et al. 1996). The results from spectral analysis with *ASCA* data also supported the interpretation of a Sedov phase SNR at  $d \sim 5$  kpc (Bai & Wang 2000).

With the relatively small angular size of the SNR ( $\sim 15'$  diameter, Busser et al. 1996) and the poor angular resolution of the data used by the previous authors, the true morphology of G299.2–2.9 could not be resolved. The *ASCA* data allowed only the analysis of

that unpublished archival *ROSAT* HRI image shows that G299.2–2.9 is in fact shell-type with bright enhancements in the northeastern portion of the shell (§ 3), which most likely caused the morphological confusion by previous authors (shell-type vs. centrally-enhanced). However, no spectral information is available with the HRI data. Spatially-resolved spectroscopy with high resolution imaging is essential to unveil the true nature of the SNR. Here we present the results from the *Chandra* observation of SNR G299.2–2.9. We describe our *Chandra* observation and the data reduction in § 2. Results from the imaging and the spectral analyses are presented in § 3 and § 4, respectively. We discuss the interpretations in § 5, and summarize the conclusions in § 6.

## 2. OBSERVATION & DATA REDUCTION

We observed G299.2–2.9 with the Advanced CCD Imaging Spectrometer (ACIS) (Garmire et al. 2003) on board *Chandra* on 2005 April 9 as part of the *Chandra* Guaranteed Time Observation program. In order to focus on the detailed study of the complex, bright, soft X-ray structure in the northeastern parts of the SNR, we used the ACIS-S3 as the primary detector by pointing at the brightest X-ray knot in the northeast. A large portion of the SNR was thus placed on the S3 chip to provide the highest available response at low energies, where the characterization of emission from O-K and Fe-L lines is particularly important for the SNR studies. Considering the angular size of  $\sim 15'$  for G299.2–2.9, we also turned on other CCDs to cover the SNR as much as possible beyond the S3 chip boundary. As we show in Fig. 1, portions of the SNR extend onto adjacent CCDs, providing nearly full coverage of the SNR. No severe variability was found in the background light curve. We corrected the spatial and spectral degradation of the ACIS data caused by radiation damage, known as the charge transfer inefficiency (CTI; Townsley et al. 2000), with the methods developed by Townsley et al. (2002a), before further standard data screening by status, grade, and energy selections. “Flaring” pixels were removed and *ASCA* grades (02346) were selected. After the data reduction, the effective exposure is 29.6 ks. The overall SNR spectrum is soft and there are few source photons above  $E \sim 3$  keV. At very low energies ( $E \lesssim 0.4$  keV), the source flux is negligible because of the foreground absorption, and X-ray emission is mostly dominated by the detector background. Thus, photons between 0.4 and 3.0 keV are extracted for the data analysis.

## 3. X-RAY MORPHOLOGY

The “X-ray-color” *Chandra* ACIS image of G299.2–2.9 is presented in Fig. 1. Our primary detector is the ACIS-S3 with the pointing roughly at the brightest X-ray knot in the northeastern part of the X-ray shell, and thus the SNR is for the most part detected on the ACIS-S3. Portions of the southern and the western boundaries are also detected on the ACIS-I3 and S4 chips. The I3 data are particularly useful by clearly imaging the bright southern shell and diffuse emission extending beyond the shell, which is similar to the features in the northern side of the SNR.

Fig. 1 shows that the overall morphology of the SNR is shell-type. We note that unpublished archival *ROSAT*

of G299.2–2.9 (Fig. 2). The brightness distribution of the *ROSAT* HRI image is dominated by a bright, almost complete shell, beyond which more diffuse emission extends to fairly large distances, in particular in the northeast. In the center of the image a low brightness patch of diffuse emission stands up above the general SNR background emission. Our *Chandra* image shows that the X-ray shell is generally soft (red to yellow in Fig. 1), and reveals complex structures such as multiple and/or broken shells, particularly in the eastern and northern sides. In general, these relatively bright, soft shell features appear to make a nearly complete circumferential shell around the SNR with an angular extent of  $\sim 10'$  in the east-west and  $\sim 9.3'$  in the north-south direction. The brightest X-ray feature in the northeastern shell of the SNR is resolved into two small knots ( $\sim 20''$ – $40''$  angular sizes) and surrounding extended features ( $\sim 1'$  sizes) (Fig. 3). These knots are located at the “connecting” or “overlapping” position of multiple shells. This morphology suggests that these bright knots may represent dense interstellar medium (ISM) along the path of the blast wave, rather than metal-rich stellar ejecta. The forward shock appears to be interacting with and wrapping around these dense, small ISM clouds. The peculiar morphology of the two bright knots surrounded by shock fronts probably suggests that the small clouds might have also been crushed by the interacting strong shock, as proposed for a similar structure seen in Puppis A SNR (Hwang et al. 2005).

Faint diffuse emission extends beyond the bright shell and appears to extend almost all around the SNR, particularly in the northern and southern portions of the SNR (Fig. 1). The angular distance between the northern and the southern boundaries of diffuse extended emission is  $\sim 13'$ . These faint emission features are also spectrally soft and, for the most part, appear to make the outer boundary of the SNR. We note that both the bright X-ray shell and faint diffuse emission extending beyond the shell appear to be nearly complete around the entire SNR. This overall morphology suggests that the blast wave is likely expanding into an inhomogeneous ISM, making two distinctive, large-scale forward shock fronts.

We detect faint diffuse emission in the central region of the SNR (Fig. 1). This central emission feature is enhanced in the Fe-L and Si-K lines (§ 4), which show a central nebulosity (Fig. 4). The *Chandra* image suggests that the faint central emission feature has an angular size of  $\sim 4'$ . Because of the low surface brightness and the partial coverage with the ACIS, however, it is difficult to accurately estimate the angular size of this central feature. We note that this central feature is reminiscent of the metal-rich ejecta nebula discovered in some middle-aged SNRs in the Magellanic Clouds (Hughes et al. 2003; Park et al. 2003a; Park et al. 2003b). Indeed, our spectral analysis of the SNR indicates the presence of overabundant heavy elements in the central nebula of G299.2–2.9 (§ 4).

## 4. SPECTRAL ANALYSIS

Spectral studies with *Chandra* have revealed that X-ray emission from SNRs is rarely described by a simple spectrum such as a single-temperature thermal plasma or the Sedov model (e.g., Weiskopf & Hughes 2005, and

SNRs typically originates from multiple-temperature plasmas in various ionization stages caused by nonequilibrium conditions in blast wave shocks propagating into an ambient medium with a wide range of interstellar density. X-ray emission from shocked, metal-rich ejecta is often detected with modern X-ray telescopes, in middle-aged SNRs as well as in young SNRs. Spatially-resolved spectral analysis from small regions within an SNR, rather than analysis of the overall integrated spectrum, is thus essential for the proper study of SNRs. We extract a number of regional spectra from G299.2–2.9 utilizing our ACIS data. There are  $\sim 30$  faint detected pointlike sources in the ACIS field of view. These point sources have been removed before extracting regional spectra. Depending on regional X-ray intensities and morphologies, we selected regions with angular sizes from  $\sim 20''$  up to a few arcminutes. We choose our regions to provide  $\sim 3000$  or more counts in each spectrum in order to place reasonable constraints on the fitted spectral parameters. We mark the representative regions of our spectral analysis in Fig. 5.

The background spectrum is estimated from source-free regions outside of the SNR’s northern (for regions on the S3 chip) and southern (for regions on the I3 chip) boundaries. Each regional source spectrum has been binned to contain a minimum of 20 counts per channel. For the spectral analysis of our CTI-corrected data, we use the response matrices appropriate for the spectral redistribution of the CCD, as generated by Townsley et al. (2002b). The CIAO `caldb` version 3.21 is used for the data processing. We use a non-equilibrium ionization (NEI) plane-parallel shock model (Borkowski et al. 2001) (`vpshock` in conjunction with the NEI version 2.0 in the `XSPEC`) which is based on `ATOMDB` (Smith et al. 2001). We use an updated version of this atomic database to include inner-shell processes that are missing in the current `XSPEC` NEI version 2.0<sup>1</sup>. The contribution of line emission from elements He, C, N, Ca, Ar, and Ni is insignificant in the fitted energy range ( $E = 0.4\text{--}3.0$  keV); thus we fix the abundances of these elements at the solar values (Anders & Grevesse 1989) (hereafter, elemental abundances are with respect to the solar). Abundances of other species (O, Ne, Mg, Si, S, and Fe) are varied freely in the fits (S abundance was occasionally fixed at 1 in cases where photon statistics are low at  $E \sim 2\text{--}3$  keV).

X-ray spectra from regions along the bright shell, and from diffuse emission beyond the shell, show characteristics consistent with emission from shock-heated ISM; on average, the thermal plasma has an electron temperature  $kT \sim 0.55$  keV and ionization timescale  $n_{\text{et}} \sim 4.5 \times 10^{11} \text{ cm}^{-3} \text{ s}$  (Fig. 6 and Table 1; errors are 90% confidence level, hereafter, unless noted otherwise.). The best-fit metal abundances are  $\sim 0.5\text{--}0.7$  for individual regions, which are marginally constrained within a factor of  $\sim 2$ . The average values of abundances from these regions are  $\text{O} = 0.63 \pm 0.28$ ,  $\text{Ne} = 0.65 \pm 0.22$ ,  $\text{Mg} = 0.54 \pm 0.19$ ,  $\text{Si} = 0.67 \pm 0.27$ , and  $\text{Fe} = 0.66 \pm 0.28$  ( $1\sigma$  errors for average values).

The absorbing column density ( $N_{\text{H}}$ ) ranges from  $\sim 2$  to  $\sim 5 \times 10^{21} \text{ cm}^{-2}$  (Table 1). The extremely low column

of  $N_{\text{H}} \sim 10^{20} \text{ cm}^{-2}$  suggested by earlier *ROSAT* data cannot fit the *Chandra* data, and is firmly rejected. Because of large statistical uncertainties (e.g., the estimated errors in Table 1 are typically  $\sim 20\text{--}30\%$  after fixing elemental abundances at the best-fit values), it is not clear whether the  $N_{\text{H}}$  variation is the true extinction variation across the SNR or statistical/systematic artifacts of the spectral fitting. For simplicity, we consider the average  $N_{\text{H}} \sim 3.5 \times 10^{21} \text{ cm}^{-2}$  in the following discussion. (We confirm that spectral fits with  $N_{\text{H}}$  fixed at this average value would not change the results with the quality of the current data.)

In contrast to the spectra from peripheral regions, faint emission from the central region reveals strong line features primarily from K-shell transitions in highly-ionized He-like Si ( $E \sim 1.85$  keV) and L-shell transitions in low-ionization-state Fe ( $E \sim 0.8 - 1$  keV) (Fig. 7). The S-K line also appears to be enhanced. The spectral analysis shows strongly overabundant Si, S, and Fe for the central region, which indicates the presence of metal-rich ejecta material produced in the core of the progenitor star. In the spectral fitting of the center region, we added an additional plane shock component in order to account for the projected contribution from the swept-up ISM in the observed spectrum. Spectral parameters for the underlying ISM component are fixed at the average values derived from our regional spectral analysis of the circumferential area (i.e.,  $kT = 0.55$  keV,  $n_{\text{et}} = 4.5 \times 10^{11} \text{ cm}^{-3} \text{ s}$ ,  $\text{O} = 0.63$ ,  $\text{Ne} = 0.65$ ,  $\text{Mg} = 0.54$ ,  $\text{Si} = 0.67$ ,  $\text{Fe} = 0.66$ ). The  $N_{\text{H}}$  was fitted, but tied in common between the ejecta and the ISM components. The best-fit  $N_{\text{H}} \sim 3.7 \times 10^{21} \text{ cm}^{-2}$  is in good agreement with the average value obtained from other regional spectral analysis. Only the normalization of the ISM component is freely varied in the fit. Results from the spectral fit of the central region are presented in Table 2. We note that the fit is not particularly good from a statistical point of view ( $\chi^2_{\nu} \sim 1.4$ ). This is not surprising for fits to complex spectra from SNRs, especially those from ejecta-dominated emission. There are uncertainties in the currently available atomic data as well as in detector calibration due to gain variation, particularly near the absorption edges and in the soft energy band ( $E \lesssim 1$  keV). In fact, the relatively high  $\chi^2$  value is dominated by a single lowest energy bin ( $E \sim 0.5$  keV) where the CCD calibration is less reliable. Detailed weak emission lines from the Fe-L complex are usually difficult to fit with low-resolution CCD spectra. The relatively large  $\chi^2$  in the central region spectral fit is most likely caused by these factors, which is beyond the usual goodness-of-fit criterion. On the other hand, the main spectral features of the broad Fe-L line emission feature and the strong Si and S lines are well-fit and provide robust measurements of spectral parameters and the abundances of key elements (O, Fe, and Si).

## 5. DISCUSSION

### 5.1. Blast Wave and Interstellar Environment

We have no reliable distance estimate to G299.2–2.9. There is no HI absorption distance measurement, which would be difficult anyway because of the faintness of the SNR in the radio band ( $< 240 \text{ mJy}$  at  $4.85 \text{ GHz}$ ). Slope

<sup>1</sup> The unpublished version of the updated model has been pro-

as measured from the spectral fit of our *Chandra* data,  $N_{\text{H}} \sim 3.5 \times 10^{21} \text{ cm}^{-2}$ , is about half of the total Galactic  $N_{\text{H}}$  in this direction (Dickey & Lockman 1990). This suggests that the SNR is neither very nearby ( $d < 1 \text{ kpc}$ ) nor extremely distant ( $d > 10 \text{ kpc}$ ). The line-of-sight in the direction of G299.2–2.9 passes through the Carina-Sagittarius spiral arm twice: once at a distance of  $\sim 2 \text{ kpc}$  and then later at a distance of  $\sim 11 \text{ kpc}$ . Assuming that the SNR is in the spiral arm or in the interarm region would be broadly consistent with the measured  $N_{\text{H}}$  distance constraint. Based on this limited amount of available independent data, we assign a plausible distance range of  $d \sim 2\text{--}11 \text{ kpc}$  to G299.2–2.9. For concreteness, we scale numerical values to  $d_5 \equiv \frac{d}{5 \text{ kpc}}$  in the following discussion, while it should be noted that the distance is uncertain by probably a factor of  $\sim 2$ .

X-ray spectra from around the shell show characteristics of hot thermal plasma from the shocked ambient ISM with normal composition. Various morphologies (e.g., the shell, filaments, knots and diffuse extended emission features with various surface brightness) then indicate that the blast wave is encountering highly inhomogeneous ambient densities. In fact, the *IRAS* 100  $\mu\text{m}$  map shows a complex interstellar environment around G299.2–2.9 (Fig. 8). The interaction of the shock with a variable density structure may also have caused the observed variation in the electron temperature and the ionization state across the SNR. The preshock density vs. electron temperature distribution from the regional spectra is largely anti-correlated (Fig. 9). In fact, the correlation coefficient for all 17 data points is  $-0.61$ , and is  $-0.82$  if the three extreme cases (regions 3, 5, and 17) are excluded. These values of the correlation coefficient imply a significant anti-correlation between the density and electron temperature (at  $>99\%$  C.L.). The preshock density  $n_0$  from each region is derived from the best-fit volume emission measure  $EM (= n_e n_{\text{H}} V$ , where  $n_e$ ,  $n_{\text{H}}$ , and  $V$  are the postshock electron density, the H density, and the emission volume assuming  $d = 5 \text{ kpc}$ , respectively). In this estimate, we assumed  $n_e = 1.2n_{\text{H}}$  for a mean charge state with normal composition and  $n_{\text{H}} = 4n_0$  for the strong shock. For the volume estimates, we assumed that the pathlengths through the regions along the line of sight are comparable with the physical sizes corresponding to the angular lengths of the regions at  $d = 5 \text{ kpc}$ . The brightest knots in the northeastern part of the shell represent low temperatures of  $kT \sim 0.35 \text{ keV}$  with the shock front entering the densest ISM,  $n_0 \sim (2\text{--}4)f^{-\frac{1}{2}} \text{ cm}^{-3}$ , where  $f$  is the volume filling factor of the X-ray emitting gas. Along the X-ray shell, except for the brightest northeastern knots, preshock densities of  $n_0 \sim (0.2\text{--}0.5)f^{-\frac{1}{2}} \text{ cm}^{-3}$  are implied. Faint diffuse emission in the northern, eastern, and southern boundaries indicates a high-temperature shock ( $kT \sim 0.7 \text{ keV}$ ) propagating into a lower density ISM ( $n_0 \lesssim 0.1f^{-\frac{1}{2}} \text{ cm}^{-3}$ ). These results indicate that the blast wave of G299.2–2.9 is expanding into more than an order of magnitude density gradient, including the densest small clouds in the northeastern side. We note that our density estimates are dependent on uncertainties involved in volume estimates. However, the volume effect is small ( $n_0 \propto V^{-\frac{1}{2}}$ ), and thus our conclusions are not strongly affected unless

magnitude.

The thin, bright filamentary emission features appear to make up a nearly complete circumferential shell around the entire SNR. On the other hand, faint diffuse emission extending beyond the bright shell forms the outermost boundary of the SNR in the north/northeastern and southern sides. Faint diffuse emission may also form the outer boundary along the western side, as suggested by the *ROSAT* HRI image (this region of the SNR was not covered by our *Chandra* observation). These two large-scale structures with the implied high and low densities suggest that the supernova might have exploded near the boundary between two regions of different ISM densities (on average,  $n_0 \lesssim 0.1 \text{ cm}^{-3}$  in one side and  $n_0 \gtrsim 0.3 \text{ cm}^{-3}$  in the other side). Each “hemisphere” might then be expanding into the relatively higher and lower ambient densities with low and high velocities, respectively, producing the observed morphology when seen in superposition along the line of sight (Fig. 10). This particular morphological development has been demonstrated by hydrodynamic simulations (Tenorio-Tagle et al. 1985). The Galactic SNR VRO 42.05.01 (G166.0+4.3) is believed to be a prototype of such a case with an edge-on orientation, which shows a peculiar two-partial shell morphology in the radio band (Pineault et al. 1987). The observed X-ray morphology of G299.2–2.9 appears to be the face-on view of the radio morphology of VRO 42.05.01. We note that, unlike G299.2–2.9, the peculiar morphology of two half-shells of VRO 42.05.01 is present only in the radio band. In X-rays, VRO 42.05.01 shows an enhancement only near the center of the SNR (Burrows & Guo 1994; Guo & Burrows 1997; Mori et al. in preparation). This is probably because of the large difference in ages between G299.2–2.9 and VRO 42.05.01; the X-ray shells of the older SNR VRO 42.05.01 ( $\tau \sim 20000 \text{ yr}$ ) might have cooled and no longer produce significant X-rays, while the relatively young ( $\tau \sim 4500 \text{ yr}$ , see below for the age estimate) G299.2–2.9’s shock is still in its hot adiabatic phase. The available archival data of G299.2–2.9 from the radio observations have only limited angular resolution of a few arcmins (e.g., Slane et al. 1996), and thus it is difficult to confirm whether the radio morphology of G299.2–2.9 also shows the same structure as seen in X-rays. Follow-up high resolution radio imaging observations should be helpful to reveal the nature of G299.2–2.9.

The angular sizes ( $\sim 9'.9$  for the bright shell,  $\sim 12'.6$  for the diffuse boundary, on average) imply physical sizes of  $\sim 14.4 d_5 \text{ pc}$  and  $\sim 18.4 d_5 \text{ pc}$  for the bright shell and the diffuse outer boundary, respectively. These large sizes of G299.2–2.9 suggest a Sedov phase for the SNR. Based on the Sedov solution, we calculate some SNR parameters of G299.2–2.9 for the two representative cases of the smaller bright shell and the larger faint rim. The derived SNR ages are  $\tau \sim 4700 d_5 \text{ yr}$  and  $4200 d_5 \text{ yr}$  for the large faint rim and the small bright shell, respectively. These results are generally consistent between the two large-scale structures. The explosion energies are estimated to be  $E_0 \sim 1.6 \times 10^{50} d_5^{\frac{5}{2}} \text{ ergs}$  for the large faint rim and  $E_0 \sim 1.7 \times 10^{50} d_5^{\frac{5}{2}} \text{ ergs}$  for the small bright shell. These  $E_0$  values are also consistent between the two cases. G299.2–2.9 is thus likely an  $\sim (4000\text{--}5000) d_5$

yr old middle-age SNR with an explosion energy of  $E_0 \sim 1.6 \times 10^{50} d_5^{\frac{5}{2}}$  ergs. The total swept-up mass,  $M_{\text{swept}}$ , is  $\sim 11 f^{\frac{1}{2}} d_5^{\frac{5}{2}} M_{\odot}$ . The SNR parameters are summarized in Table 3.

### 5.2. Metal-Rich Ejecta

The central emission feature is faint, and appears to have an average radius of  $\sim 2'$ , showing spectral characteristics entirely different from those of the circumferential regions. The electron temperature is high ( $kT \sim 1.36$  keV) with a low ionization timescale ( $n_e t \sim 1.3 \times 10^{10} \text{ cm}^{-3} \text{ s}$ ). The strong line emission from the elemental species of Si, S, and Fe reveals enhancements in the abundances of those elements. These results indicate that the central region of G299.2–2.9 is most likely the ejecta nebula, i.e., emission from low density metal-rich ejecta material heated by the reverse shock. Our spectral analysis indicates that the ejecta is enriched particularly in the heavy Si-group species produced in the deep core of the progenitor star. The detection of Si- and Fe-rich ejecta in the central region of the SNR is reminiscent of the Type Ia SNR DEM L71 in the Large Magellanic Cloud (Hughes et al. 2003). In analogy to DEM L71, we propose that G299.2–2.9 is a Type Ia SNR.

To investigate this suggestion further, we compare the observed Si to Fe mass ratio with the standard Type Ia/II supernova nucleosynthesis models, estimating the mass ratio  $M_{\text{Si}}/M_{\text{Fe}}$  from the best-fit  $EM$  ratio of the center region. Based on the dominant ionization states of the Si and Fe implied by the observed spectrum, we assume that the electron densities associated with the Si and Fe ions are  $n_{e,\text{Si}} \sim 12 n_{\text{Si}}$  and  $n_{e,\text{Fe}} \sim 18 n_{\text{Fe}}$ , for simple “pure” Si and Fe ejecta cases, respectively. For the dominant isotopes of  $^{28}\text{Si}$  and  $^{56}\text{Fe}$ , the measured Si and Fe abundances imply  $M_{\text{Si}}/M_{\text{Fe}} = 0.52^{+0.20}_{-0.15} (V_{\text{Si}}/V_{\text{Fe}})^{\frac{1}{2}}$ . Therefore, if the Fe and Si occupy the same size volumes ( $V_{\text{Fe}} = V_{\text{Si}}$ ), the mass ratio is  $M_{\text{Si}}/M_{\text{Fe}} \sim 0.52$ . In the case of DEM L71,  $V_{\text{Si}}$  is a thick shell extending only about half way to the center of the SNR, while Fe is present even at the center of the SNR. If we assume such a stratified ejecta structure for G299.2–2.9,  $V_{\text{Si}}/V_{\text{Fe}}$  is  $\sim 0.88$  and thus  $M_{\text{Si}}/M_{\text{Fe}} \sim 0.49$ . If  $V_{\text{Si}}$  corresponds to a thinner shell,  $M_{\text{Si}}/M_{\text{Fe}}$  becomes only smaller. These small Si to Fe mass ratios are in good agreement with Type Ia supernova models (Nomoto et al. 1997b). For Type II cases, the Si to Fe mass ratio is typically large ( $\sim 1$ – $10$ , for progenitor masses of  $18$ – $70 M_{\odot}$ ) (Nomoto et al. 1997a). We note that, in the case of a *complete* spatial mixture of Si and Fe (i.e.,  $n_{e,\text{Si}} \approx n_{e,\text{Fe}}$ ),  $M_{\text{Si}}/M_{\text{Fe}}$  becomes  $\sim 20\%$  smaller. Such a case may be implied by the assumption of  $V_{\text{Fe}} = V_{\text{Si}}$ , but the actual  $n_{e,\text{Si}}$  and  $n_{e,\text{Fe}}$  distributions may depend on the details of the geometrical structure of the ejecta material. Nonetheless, these details of the ejecta structure would not affect our general conclusions. We also note that the mixture of H in the metal-rich ejecta may not affect our mass ratio estimates, as long as the H mixture rates are comparable between the Fe and the Si ejecta.

Although  $M_{\text{Si}}/M_{\text{Fe}} \lesssim 0.5$  may also be consistent with a Type II case for a relatively less massive progenitor ( $< 15 M_{\odot}$ ) (Nomoto et al. 1997a), the lack of any

a Type II origin. Unlike the case of the Si- and Fe-rich ejecta, we find no evidence of enhancements for the light species, O, Ne, and Mg. For instance, the fitted O abundance is negligible ( $< 0.1$ ), suggesting that the Fe to O abundance ratio is high ( $> 4$ ). The Si to O abundance ratio is also high ( $> 3$ ). These high Fe and Si abundances relative to the O abundance are consistent with Type Ia cases ( $\sim 1$ – $5$ ), while Fe/O and Si/O ratios are at least an order of magnitude lower for Type II supernovae (Nomoto et al. 1997a; Nomoto et al. 1997b).

## 6. SUMMARY AND CONCLUSIONS

We present results from the *Chandra* observation of the Galactic SNR G299.2–2.9. High resolution images from the *Chandra* observation confirm a shell-type morphology for the SNR. In addition to the bright X-ray shell, we detect faint diffuse emission which extends beyond the shell to define the outer boundary nearly all around the SNR. Our spatially-resolved spectral analysis of the SNR indicates that the blast wave of G299.2–2.9 is expanding into a highly inhomogeneous ISM with ambient densities varying over more than an order of magnitude, including several small ISM clouds with densities of  $\sim 2$ – $4 \text{ cm}^{-3}$  that have been engulfed by the blast wave. Bright shell emission (excluding the clouds) originates from shocked interstellar material with preshock densities of  $n_0 \sim 0.2$ – $0.5 \text{ cm}^{-3}$ . Faint extended emission beyond the shell comes from a lower density medium ( $n_0 \lesssim 0.1 \text{ cm}^{-3}$ ) also heated by the blast wave. These morphological and spectral characteristics suggest to us that the supernova exploded within a region with a large-scale gradient in ambient density, perhaps even near the boundary between two distinct density regions of the ISM. In this scenario, the blast wave will expand at a higher velocity into the lower density ISM than into the higher density, which will result in two “hemispheres” with different sizes that, if viewed from the side, might have a morphology that is schematically shown in Fig. 10. G299.2–2.9 may represent a nearly face-on view of such a configuration.

How do our derived ambient density values compare with expectations? The density of the interstellar medium is a strong function of  $z$  distance above the Galactic plane. Given the SNR’s location  $2.9^\circ$  below the plane, its  $z$  distance varies from  $\sim 100$  pc to  $\sim 500$  pc for distances between 2 and 10 kpc. In a recent review, Ferrière (2001) provides analytical relations for the  $z$ -height variation of various constituents of the ISM in the Milky Way. Using these relations we determine the expected ambient number density to be  $\sim 0.4 \text{ cm}^{-3}$  for  $z = 100$  pc (corresponding to a distance of 2 kpc) and  $\sim 0.03 \text{ cm}^{-3}$  for  $z = 500$  pc (distance of 10 kpc). The midpoint distance of 5 kpc yields an expected ambient density of  $\sim 0.1 \text{ cm}^{-3}$  that is in good agreement with our X-ray measurements.

The central region of G299.2–2.9 shows faint diffuse emission with strong line emission from Si, S, and Fe. This central region is most likely metal-rich stellar ejecta heated by the reverse shock. The ejecta are enriched in Si and Fe, while showing no evidence for enhancement in the light elements O and Ne. The inferred mass of Si in the ejecta is roughly half that of the Fe ejecta. This abundance pattern in the central ejecta suggests a Type

Fe and Si species, however, cannot be determined with the current data. Deeper X-ray observations, covering the entire SNR, would allow a more detailed study of this rare Galactic example of a middle-aged Type Ia SNR<sup>2</sup>.

We have used the X-ray temperatures, sizes, and density measurements to estimate the age and explosion energy of the originating SN under the assumption that the SNR is currently in the Sedov phase of evolution. This calculation was carried out separately for both the faint and bright portions of the shell, which provided consistent values. G299.2–2.9 is middle-aged ( $\tau \sim 4500$  yr) with a supernova explosion energy of  $E_0 \sim 1.6 \times 10^{50}$  ergs, if the SNR is located at the midpoint value (5 kpc) of our plausible range of distances. This value for the explosion energy is rather low – most SN explosion models predict  $10^{51}$  ergs in the kinetic energy of the ejecta. If

G299.2–2.9 were as distant as 10 kpc, then the explosion energy would increase to a more reasonable value of  $E_0 \sim 9 \times 10^{50}$  (and the age would become  $\sim 9000$  yr). However, at this distance, there would be poorer agreement between the X-ray–inferred ambient medium density ( $n_0 \sim 0.07 \text{ cm}^{-3}$ ) and the expected value of  $\sim 0.03 \text{ cm}^{-3}$  (see preceding paragraph). Given the current state of knowledge, the situation is inconclusive. A strong constraint on the distance to G299.2–2.9 is going to be required before concluding that the originating SN was sub-energetic.

The authors thank K. Borkowski for providing us the updated NEI models. This work was supported in part by SAO under *Chandra* grant SV4-74018. POS acknowledges support from NASA contract NAS8-39073.

<sup>2</sup> While completing this work, we became aware of an independent study by L. Pittroff et al. on the *XMM-Newton* observations of this same SNR. The main conclusions reached here appear con-

sistent with their preliminary results.

#### REFERENCES

- Anders, E. & Grevesse, N. 1989, *Geochim. Cosmochim. Acta*, 53, 197
- Bai, L. & Wang, Z.-R. 2000, *ApJ*, 539, 760
- Borkowski, K. J., Lyerly, W. J., & Reynolds, S. P. 2001, *ApJ*, 548, 820
- Burrows, D. N. & Guo, Z. 1994, *ApJ*, 421, L19
- Busser, J.-U., Egger, R. & Aschenbach, B. 1995, *IAU Circ.* 6142
- Busser, J.-U., Egger, R. & Aschenbach, B. 1996, *A&A*, 310, L1
- Dickey, J. M. & Lockman, F. J. 1990, *ARA&A*, 28, 215
- Ferrière, K. M. 2001, *RvMP*, 73, 1031
- Garmire, G. P., Bautz, M. W., Ford, P. G., Nousek, J. A., & Ricker, Jr., G. R. 2003, in “X-Ray and Gamma-Ray Telescopes and Instruments for Astronomy”, *Proc. of SPIE*, eds. J. E. Trümper and H. D. Tananbaum, 4851, 28
- Guo, Z. & Burrows, D. N. 1997, *ApJ*, 480, L51
- Hughes, J. P., Ghavanian, P., Rakowski, C. E. & Slane, P. O. 2003, *ApJ*, 582, L95
- Hwang, U., Flanagan, K. A., & Petre, R. 2005, *ApJ*, 635, 355
- Lockman, F. J. 1984, *ApJ*, 283, 90
- Nomoto, K., Hashimoto, M., Tsujimoto, T., Thielemann, F.-K., Kishimoto, N., Kubo, Y., & Nakasato, N. 1997a, *Nucl. Phys. A*, 616, 79
- Nomoto, K., Iwamoto, K., Nakasato, N., Thielemann, F.-K., Brachwitz, F., Tsujimoto, T., Kubo, Y., & Kishimoto, N. 1997b, *Nucl. Phys. A*, 621, 467
- Park, S., Hughes, J. P., Slane, P. O., Burrows, D. N., Warren, J. S., Garmire, G. P. & Nousek, J. A. 2003a, *ApJ*, 592, L41
- Park, S., Hughes, J. P., Burrows, D. N., Slane, P. O., Nousek, J. A. & Garmire, G. P. 2003b, *ApJ*, 598, L95
- Pineault, S., Landecker, T. L., & Routledge, D. 1987, *ApJ*, 315, 580
- Slane, P. O., Vancura, O., & Hughes, J. P. 1996, *ApJ*, 465, 840
- Smith, R. K., Brickhouse, N. S., Liedahl, D. A., & Raymond, J. C. 2001, *ApJ*, 556, L91
- Tenorio-Tagle, G., Bodenheimer, P., & Yorke, H. W. 1985, *A&A*, 145, 70
- Townsley, L. K., Broos, P. S., Garmire, G. P., & Nousek, J. A. 2000, *ApJ*, 534, L139
- Townsley, L. K., Broos, P. S., Chartas, G., Moskalenko, E., Nousek, J. A., & Pavlov, G. G. 2002a, *Nucl. Instrum. Methods Phys. Res. A*, 486, 716
- Townsley, L. K., Broos, P. S., Nousek, J. A., & Garmire, G. P. 2002b, *Nucl. Instrum. Methods Phys. Res. A*, 486, 751
- Weisskopf, M. C. & Hughes, J. P. 2005, *Astrophysics Update* 2, ed. J. W. Mason, (Springer: Berlin), 55
- White, R. L. & Long, K. S. 1991, *ApJ*, 373, 543

TABLE 1  
BEST-FIT PARAMETERS FROM THE SPECTRAL MODEL FIT OF THE SHELL REGIONS OF  
G299.2–2.9

Region	$N_H^a$ ( $10^{21}$ cm $^{-2}$ )	$kT^a$ (keV)	$n_e t^a$ ( $10^{11}$ cm $^{-3}$ s)	$EM^a$ ( $10^{56}$ cm $^{-3}$ )	$V^b$ ( $10^{55}$ cm $^3$ )	$\chi^2/\nu$
1	$2.6^{+1.1}_{-1.1}$	$0.54^{+0.13}_{-0.14}$	$1.42^{+1.20}_{-0.42}$	$1.03^{+1.08}_{-0.30}$	45.6	61.3/54
2	$4.6^{+0.7}_{-0.8}$	$0.34^{+0.08}_{-0.06}$	$3.12^{+6.21}_{-1.24}$	$6.09^{+6.00}_{-3.03}$	10.4	78.7/58
3	$4.6^{+0.7}_{-0.6}$	$0.35^{+0.07}_{-0.06}$	$5.53^{+16.50}_{-2.15}$	$6.84^{+5.85}_{-2.79}$	0.3	62.2/61
4	$2.5^{+0.6}_{-0.6}$	$0.68^{+0.08}_{-0.07}$	$0.84^{+0.57}_{-0.30}$	$0.70^{+0.23}_{-0.12}$	24.1	54.0/58
5	$4.2^{+0.6}_{-0.7}$	$0.36^{+0.08}_{-0.07}$	$> 5.27$	$6.00^{+4.35}_{-2.67}$	0.8	56.0/62
6	$3.5^{+0.8}_{-0.7}$	$0.56^{+0.06}_{-0.07}$	$1.56^{+0.75}_{-0.59}$	$1.63^{+0.83}_{-0.35}$	8.7	59.2/63
7	$3.7^{+0.7}_{-0.8}$	$0.40^{+0.08}_{-0.06}$	$2.00^{+1.40}_{-0.75}$	$3.21^{+2.42}_{-1.39}$	8.7	77.8/57
8	$3.5^{+0.7}_{-0.5}$	$0.53^{+0.03}_{-0.05}$	$8.88^{+3.82}_{-2.74}$	$1.47^{+0.46}_{-0.25}$	12.2	77.8/66
9	$3.1^{+0.6}_{-0.6}$	$0.71^{+0.10}_{-0.09}$	$0.72^{+0.55}_{-0.29}$	$0.64^{+0.28}_{-0.12}$	7.2	64.1/57
10	$3.0^{+0.8}_{-0.6}$	$0.52^{+0.05}_{-0.06}$	$2.51^{+1.10}_{-0.93}$	$1.39^{+0.62}_{-0.32}$	6.3	60.5/60
11	$3.1^{+0.5}_{-0.4}$	$0.58^{+0.03}_{-0.02}$	$14.60^{+7.61}_{-4.57}$	$1.35^{+0.20}_{-0.15}$	11.1	78.6/66
12	$1.7^{+0.7}_{-0.5}$	$0.56^{+0.04}_{-0.07}$	$4.53^{+1.71}_{-1.49}$	$0.68^{+0.23}_{-0.11}$	19.3	80.4/58
13	$2.4^{+0.4}_{-0.4}$	$0.64^{+0.03}_{-0.02}$	$4.51^{+1.49}_{-1.24}$	$1.07^{+0.14}_{-0.10}$	13.4	77.0/70
14	$2.9^{+0.6}_{-0.5}$	$0.57^{+0.02}_{-0.03}$	$7.35^{+2.39}_{-2.06}$	$1.36^{+0.25}_{-0.18}$	12.3	100.3/68
15	$3.3^{+0.7}_{-0.6}$	$0.57^{+0.03}_{-0.05}$	$5.99^{+3.05}_{-1.97}$	$1.15^{+0.33}_{-0.19}$	14.3	63.4/62
16	$3.6^{+0.5}_{-0.5}$	$0.63^{+0.07}_{-0.06}$	$1.67^{+0.79}_{-0.57}$	$2.80^{+0.77}_{-0.51}$	32.4	113.8/67
17	$3.1^{+0.8}_{-0.6}$	$0.88^{+0.28}_{-0.19}$	$0.54^{+0.49}_{-0.21}$	$1.27^{+0.68}_{-0.38}$	205.4	42.6/55

<sup>a</sup>The errors are estimated with the elemental abundances fixed at the best-fit values. The fitted mean abundances are O =  $0.63 \pm 0.28$ , Ne =  $0.65 \pm 0.22$ , Mg =  $0.54 \pm 0.19$ , Si =  $0.67 \pm 0.27$ , and Fe =  $0.66 \pm 0.28$ .

<sup>b</sup>Emission volume (assuming  $d = 5$  kpc) used to calculate the density for each region.

TABLE 2  
BEST-FIT PARAMETERS FROM THE SPECTRAL MODEL FIT OF THE CENTRAL NEBULA OF G299.2–2.9

$N_H^a$ ( $10^{21}$ cm $^{-2}$ )	$kT^a$ (keV)	$n_e t^a$ ( $10^{11}$ cm $^{-3}$ s)	$EM^a$ ( $10^{56}$ cm $^{-3}$ )	Si <sup>b</sup>	S <sup>b</sup>	Fe <sup>b</sup>	$\chi^2/\nu$
$3.7^{+0.3}_{-0.3}$	$1.36^{+0.03}_{-0.13}$	$0.13^{+0.03}_{-0.03}$	$0.25^{+0.08}_{-0.06}$	$7.25^{+1.84}_{-1.42}$	$19.59^{+6.69}_{-5.31}$	$7.72^{+2.32}_{-1.79}$	85.6/60

<sup>a</sup>The errors are estimated with the elemental abundances fixed at the best-fit values.

<sup>b</sup>The best-fit abundances with respect to the solar. The fitted abundances for other elements (O, Ne, and Mg) are low ( $\lesssim 0.6$ ) and have been fixed before estimating the  $1\sigma$  uncertainties for Si, S, and Fe.

TABLE 3  
SNR PARAMETERS OF G299.2–2.9

Parameter	Bright Shell	Faint Rim	Entire SNR <sup>a</sup>
$kT$ (keV)	$0.52 \pm 0.04^b$	$0.67 \pm 0.04^c$	-
$R$ ( $d_5$ pc)	7.2	9.2	-
$n_e$ ( $f^{-\frac{1}{2}} d_5^{-\frac{1}{2}} \text{ cm}^{-3}$ )	$1.58 \pm 0.16$	$0.50 \pm 0.06$	-
$n_0$ ( $f^{-\frac{1}{2}} d_5^{-\frac{1}{2}} \text{ cm}^{-3}$ )	$0.33 \pm 0.03$	$0.11 \pm 0.01$	-
$E_0$ ( $d_5^{\frac{5}{2}} f^{-\frac{1}{2}} 10^{50} \text{ ergs}$ )	$1.71 \pm 0.22$	$1.55 \pm 0.20$	$1.63 \pm 0.21$
Age ( $d_5 \text{ yr}$ )	$4200 \pm 170$	$4700 \pm 140$	$4500 \pm 160$
$M_{\text{swept}}$ ( $f^{\frac{1}{2}} d_5^{\frac{5}{2}} M_{\odot}$ )	$12.8 \pm 1.3$	$8.8 \pm 1.0$	$10.8 \pm 1.1$

NOTE. —  $1\sigma$  uncertainties are quoted.

<sup>a</sup>Mean values of the two assumed cases.

<sup>b</sup>On average based on the spectral fits from the bright shell (i.e., regions 2, 6–7, 10, 13–14, and 16). The brightest northeastern knots (regions 3 and 5) are excluded.

<sup>c</sup>On average based on the spectral fits from the faint outer boundary (i.e., regions 1, 4, 12, and 17).



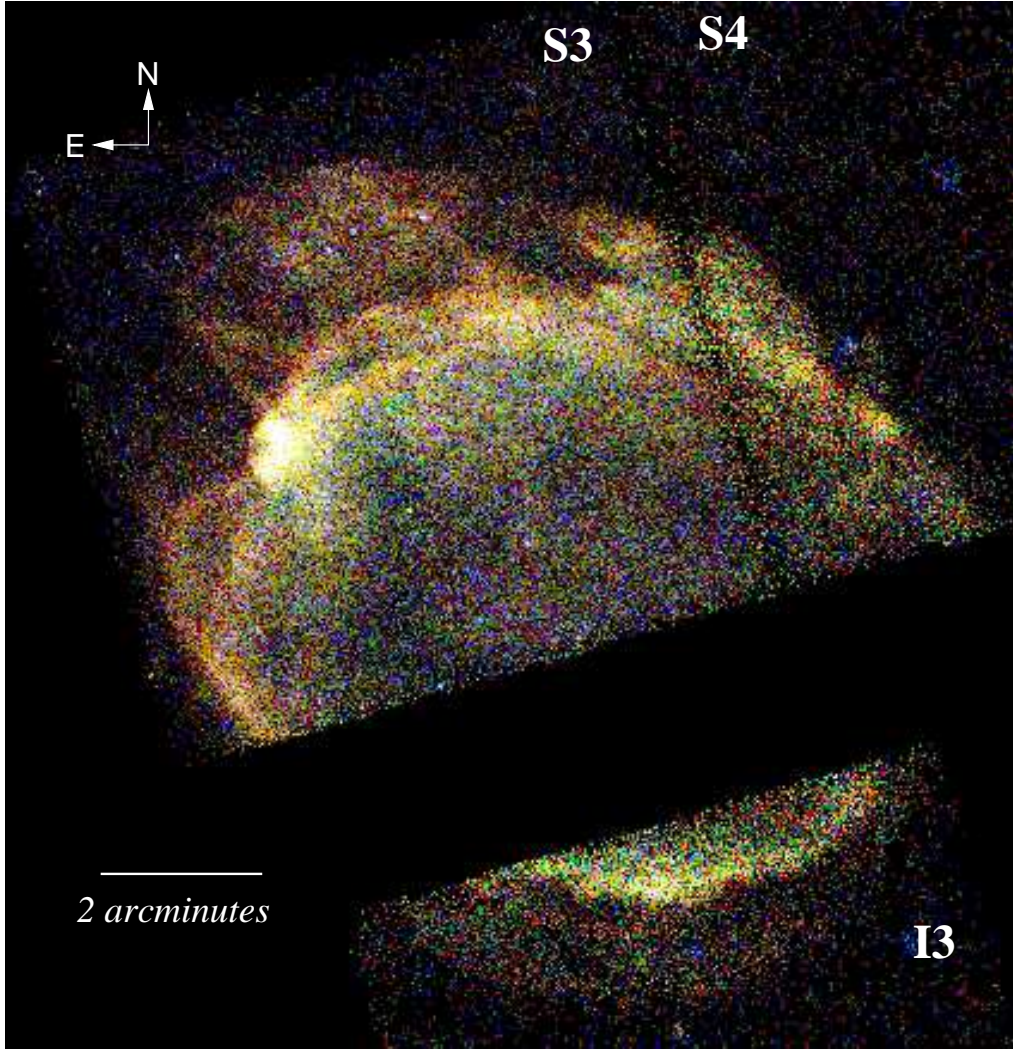


FIG. 1.— Three-color image of G299.2-2.9: Red is 0.4 – 0.9 keV, green is 0.9 – 1.4 keV, and blue is 1.4 – 3.0 keV. Each subband image has been corrected for the exposure and the detector efficiency. The images have been binned by 4 pixels for the purpose of display.

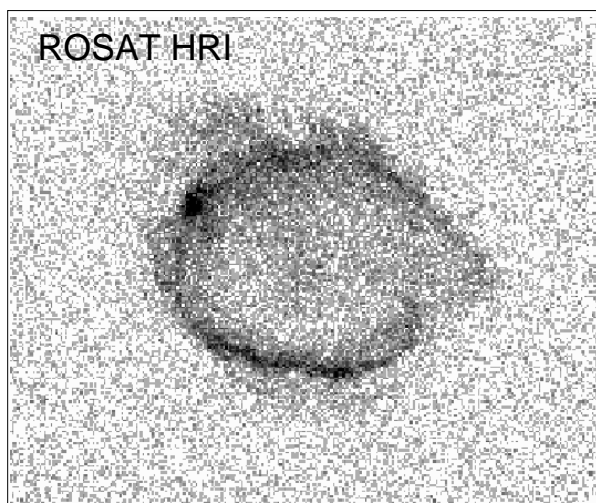


FIG. 2.— The archival *ROSAT* HRI image of G299.2–2.9 (taken from the *SkyView* service by the HEASARC), showing the SNR in its entirety.

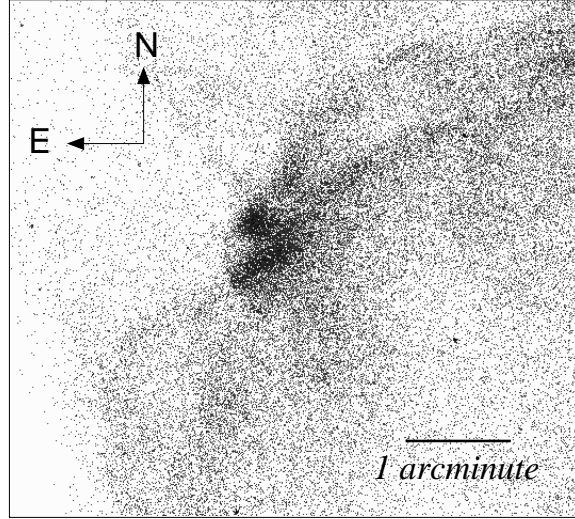


FIG. 3.— The full-resolution ( $0''.5$ ) broadband ACIS image of the region around the brightest knots in the northeastern shell. Darker grey-scales correspond to higher intensities.

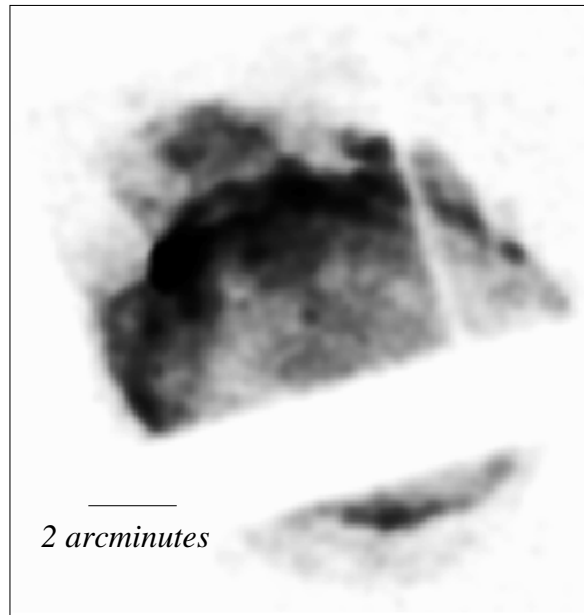


FIG. 4.— The combined image of Fe ( $0.75 - 0.95$  keV) and Si ( $1.75 - 1.95$  keV) lines of G299.2–2.9. The image has been binned into  $6 \times 6$  pixels and then smoothed with a Gaussian ( $\sigma = 3$  pixels) for the purposes of display. In order to emphasize the faint central ejecta nebula, the bright shell regions are saturated in dark grey-scales.

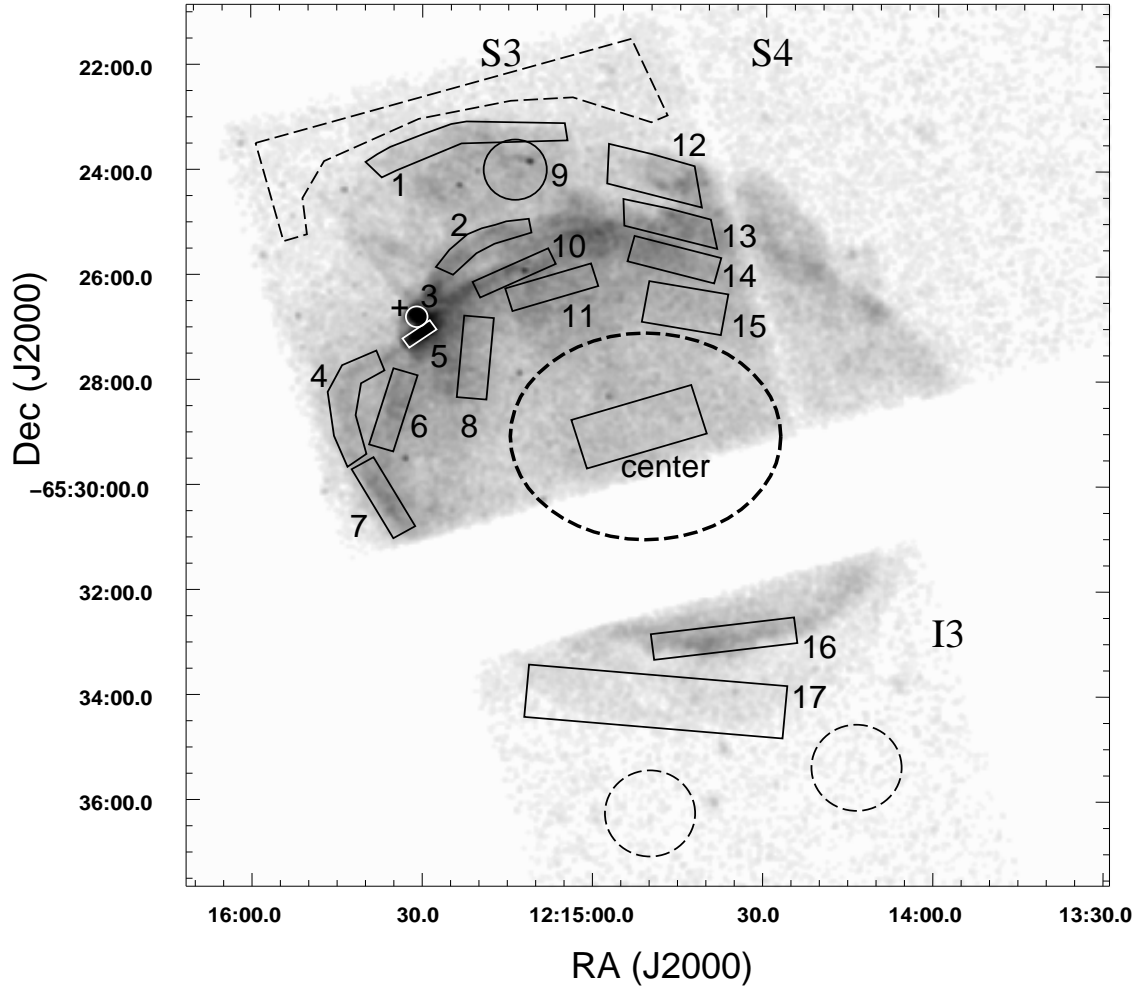


FIG. 5.— The gray-scale broad band (0.4 – 3.0 keV) image of G299.2–2.9 from the *Chandra*/ACIS observation. The image has been binned with 2 pixels and then smoothed by a Gaussian ( $\sigma = 5$  pixels) for the purposes of display. The small regions used for the spectral analysis (Table 1) are marked with solid boxes and circles. The thick dashed ellipse schematically indicates the faint diffuse central emission feature enriched in Si and Fe. The pointing direction is marked with a cross, just outside of the brightest knot (region 3) on the S3 chip. The background was estimated with emission from the thin dashed regions.

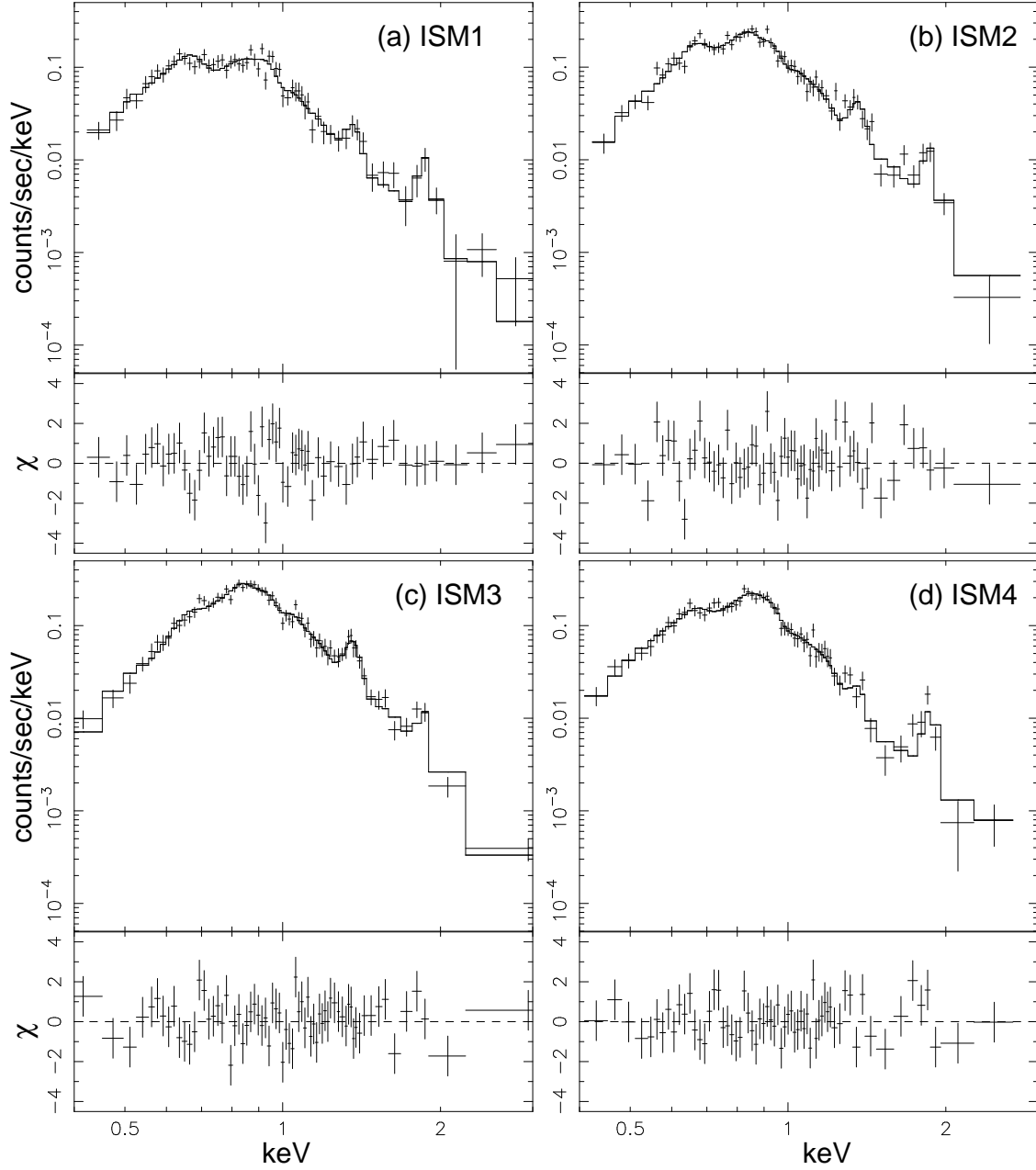


FIG. 6.— The regional ACIS spectra of G299.2–2.9. Four representative spectra from the shocked ISM regions. Panels (a), (b), (c), and (d) correspond to regions 1, 2, 3, and 4 in Fig. 5, respectively. The best-fit planar shock model is overlaid in each panel. The lower plot in each panel is the residuals from the best-fit model.

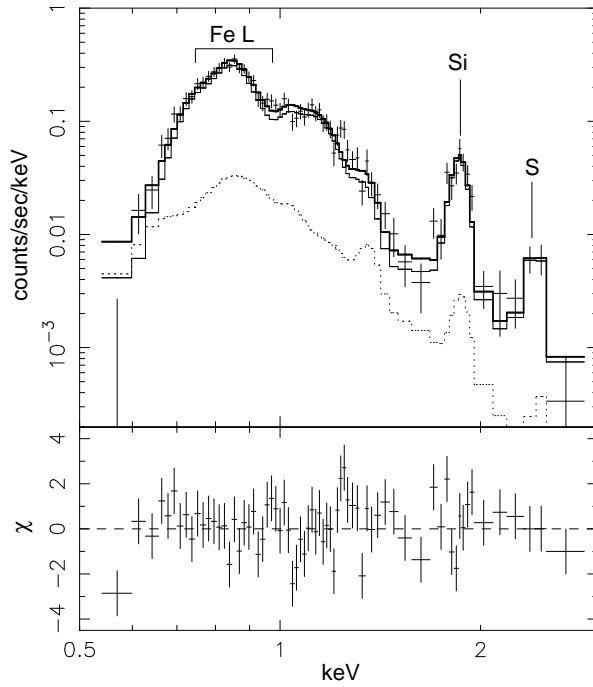


FIG. 7.— The spectrum of G299.2–2.9 from the center region. The dotted line is the model for the contribution from the projected shocked ISM component, and the thin solid line is the central ejecta component. The best-fit model (ejecta + ISM) is overlaid with the thick solid line. The lower plot is the residuals from the best-fit model.

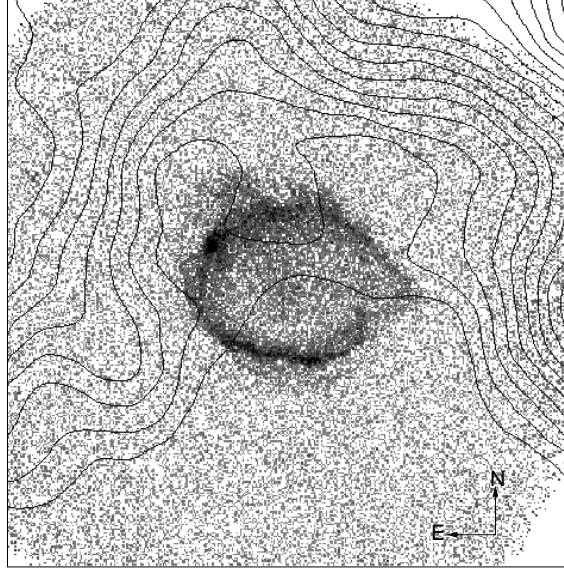


FIG. 8.— The gray-scale *ROSAT* HRI image of G299.2–2.9, overlaid with the *IRAS* 100  $\mu\text{m}$  contours. The *IRAS* 100  $\mu\text{m}$  image was taken from the *SkyView* services provided by the HEASARC. The Galactic plane is toward the north.

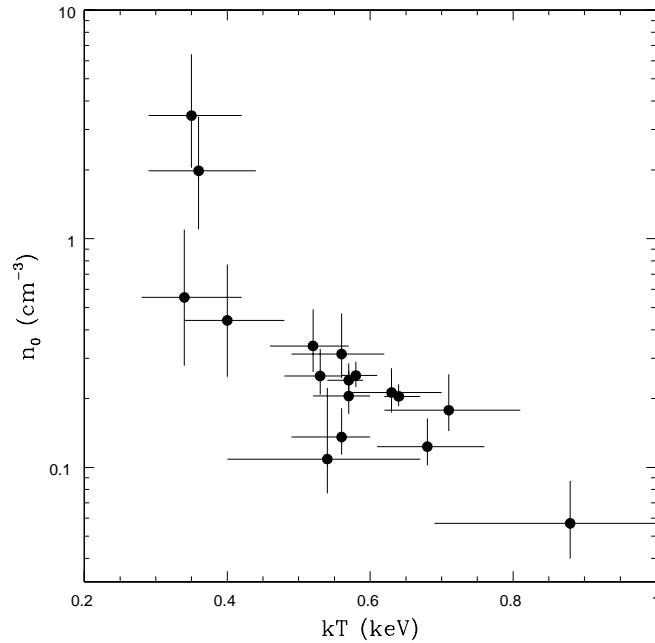


FIG. 9.—  $kT$  vs.  $n_0$  distribution from the best-fit spectral models of the regional spectra of G299.2–2.9, taken from the regions marked in Fig. 5.  $n_0$  is calculated from the best-fit  $EM$  from each regional spectral fit as described in the text. 17 regions (out of the total 21) showing normal abundances are presented. The errors are estimated with the elemental abundances fixed at the best-fit values.

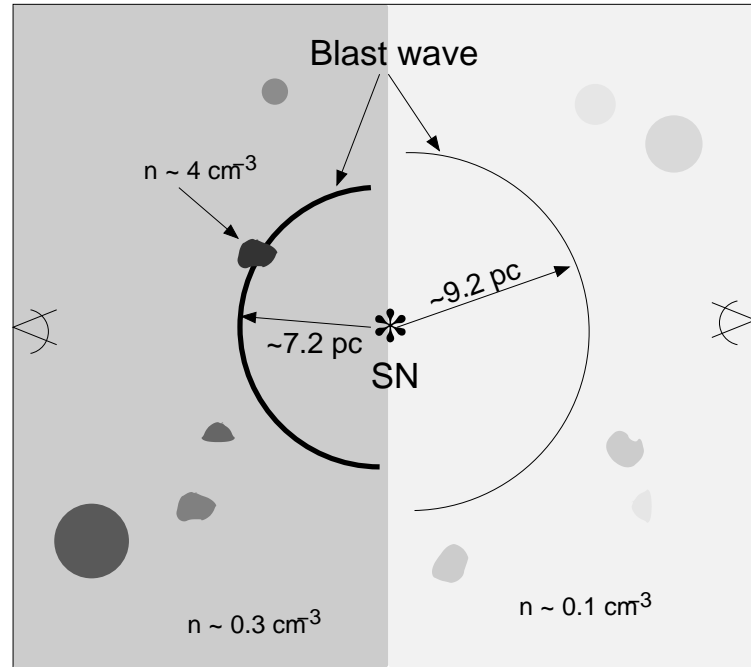


FIG. 10.— A schematic “edge-on” view of G299.2–2.9.